Supporting Information

Chiral Assembly of Dodecahedral Cavities into Porous Metal-Organic Frameworks

Hui Yang[a,b], Fei Wang[a], Yao Kang[a], Tie-Hu Li [b] and Jian Zhang* [a,]

[a]State Key Laboratory of Structural Chemistry, Fujian Institute of Research on the Structure of Matter, Chinese Academy of Sciences, Fuzhou, Fujian 350002, P. R. China.
[b] School of Materials Science and Engineering, Northwestern Polytechnical University, Xi'an, China 710072
Email: zhj@fjirsm.ac.cn

Experimental Section

Materials and Instrumentation: All reagents were purchased commercially and used without further purification. All syntheses were carried out in 23 ml polytetrafluoroethylene lined stainless steel containers under autogenous pressure. FT-IR spectra were measured as KBr pellets on a Nicolet Magna 750 FT-IR spectrometer in the range of 400~4000 cm^{-1}. Elemental analysis (EA) was measured on a vario MICRO. All Powder X-ray diffraction (PXRD) analyses were recorded on a Rigaku Dmax2500 diffractometer with Cu Kα radiation ($\lambda = 1.54056$ Å) with a step size of 0.05°. Thermal stability studies were carried out on a NETSCHZ STA-449C thermoanalyzer with a heating rate of 10 °C/min under an air atmosphere. Gas adsorption measurement was performed in the ASAP (Accelerated Surface Area and Porosimetry) 2020 System. The content of copper and zinc (**2**) was measured by inductively coupled plasma atomic emission spectroscopy (ICP-AES). The valence of copper (**2**) was measured by X-ray photoelectron spectroscopy (XPS).
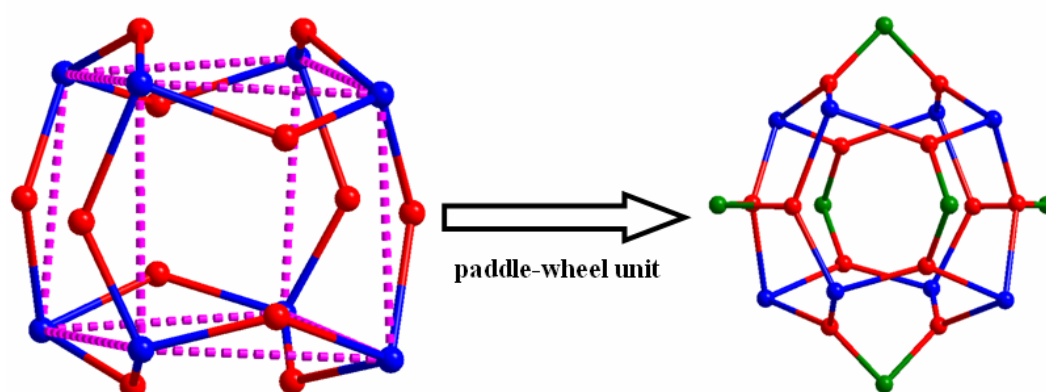

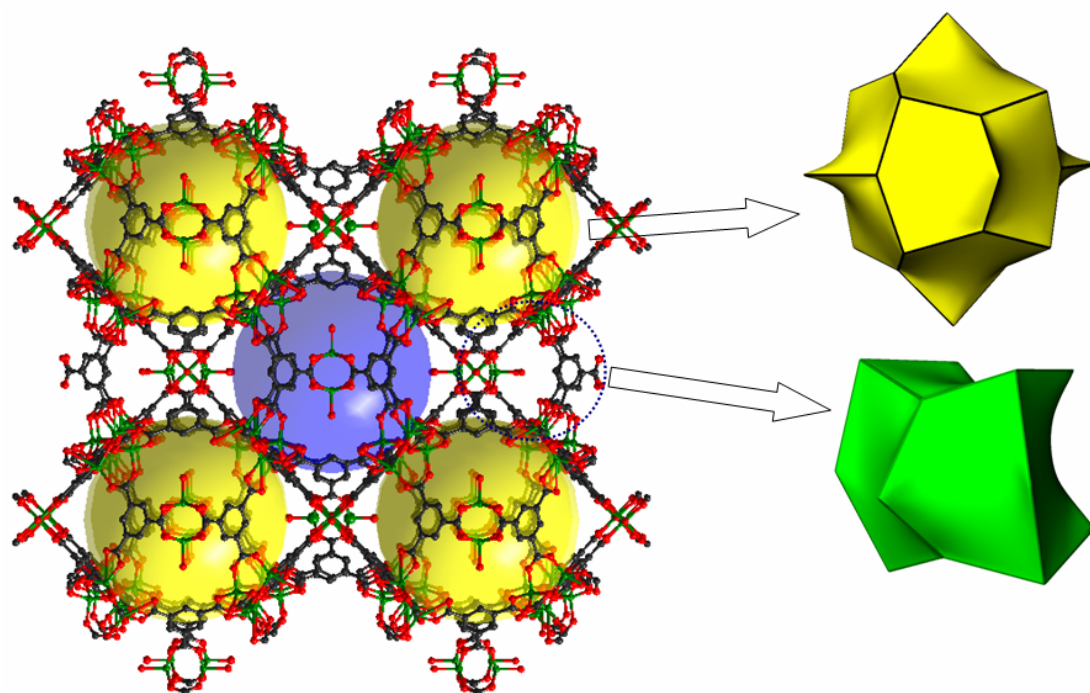Figure S1. From cubic cavity turned into dodecahedral cavity in **1**.

2

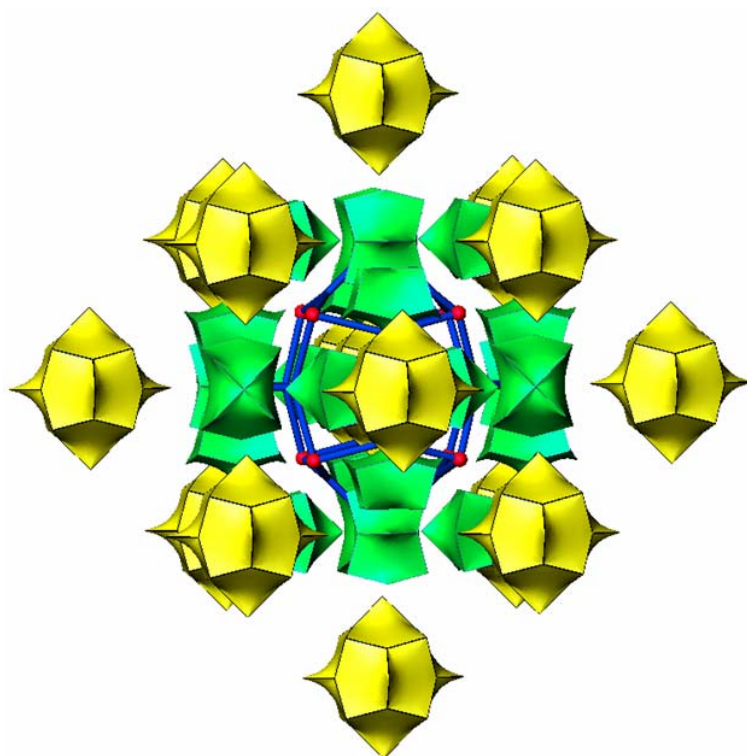Figure S2. The dodecahedron and hexahedral cavities in **1.**

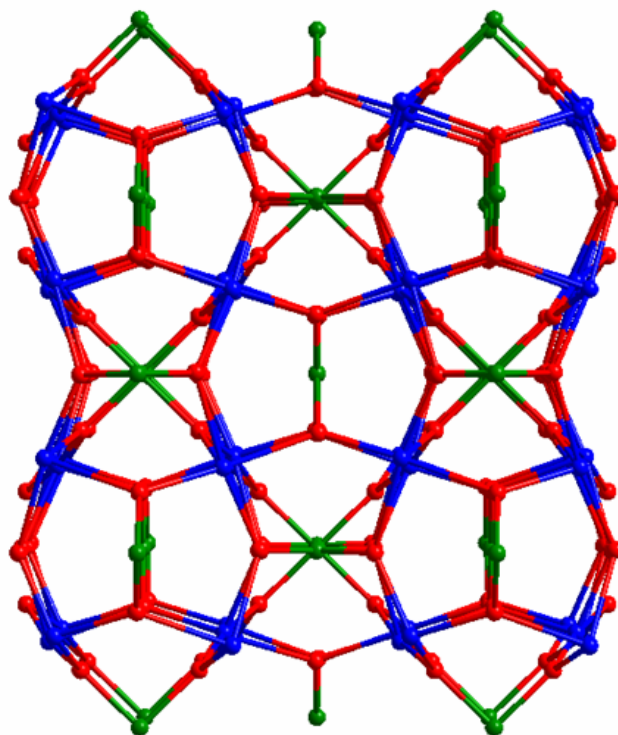Figure S3. Its natural tiling showing the packing of the structures in **1**.
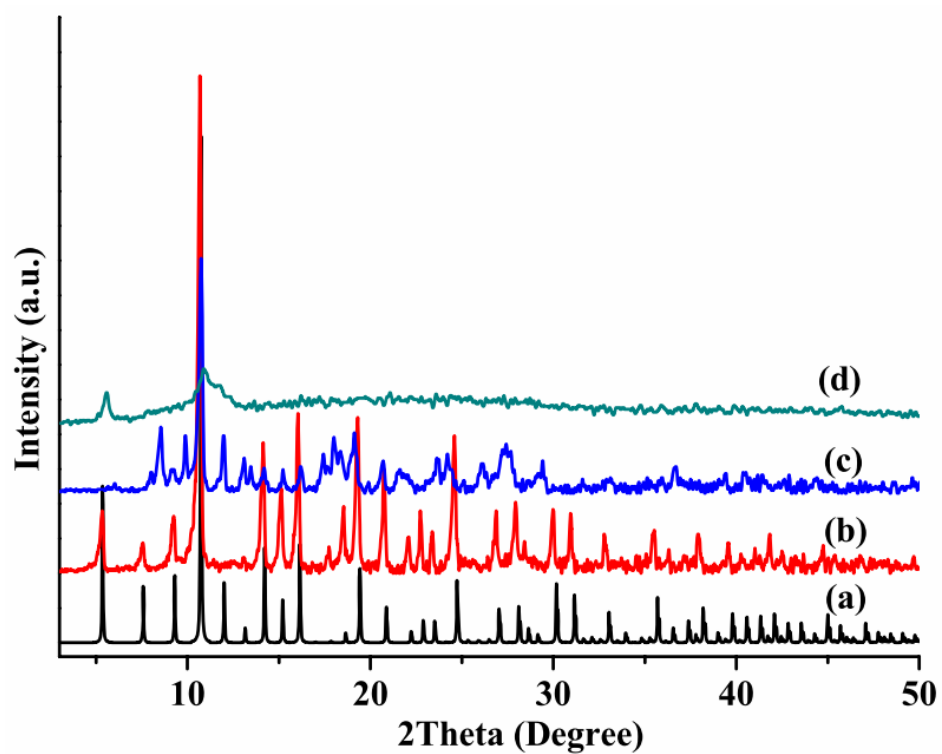
Figure S4. Topological representation of **1**.

Figure S5. The Powder XRD pattern of **1**: (a) simulated; (b) experiment; (c) soaked in MeOH; (d) after activation.
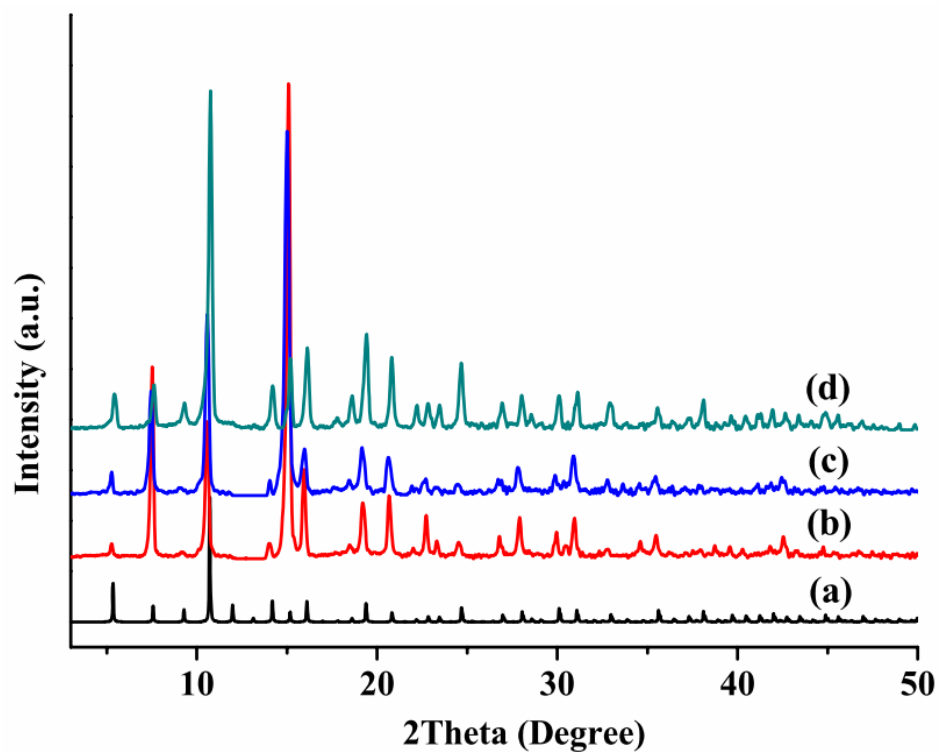
4

Figure S6. The Powder XRD pattern of **2**: (a) simulated; (b) experiment; (c) soaked in MeOH; (d) after adsorption.
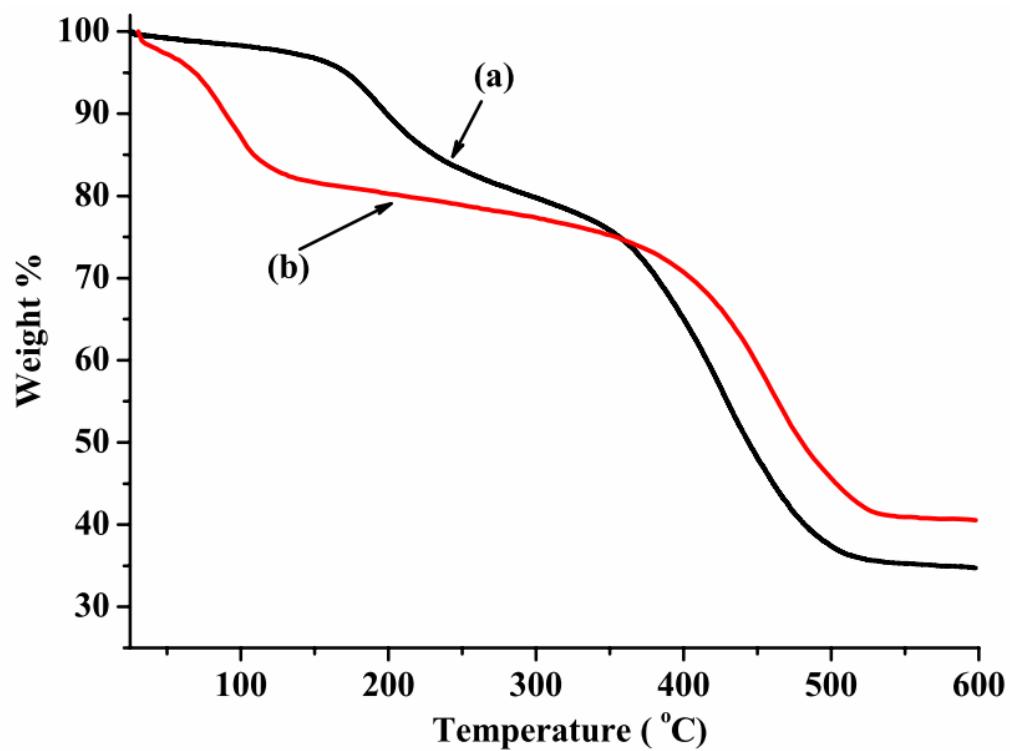

Figure S7. The TGA diagrams of **1** (a, black); The TGA diagrams of **1** soaked in MeOH (b, red).
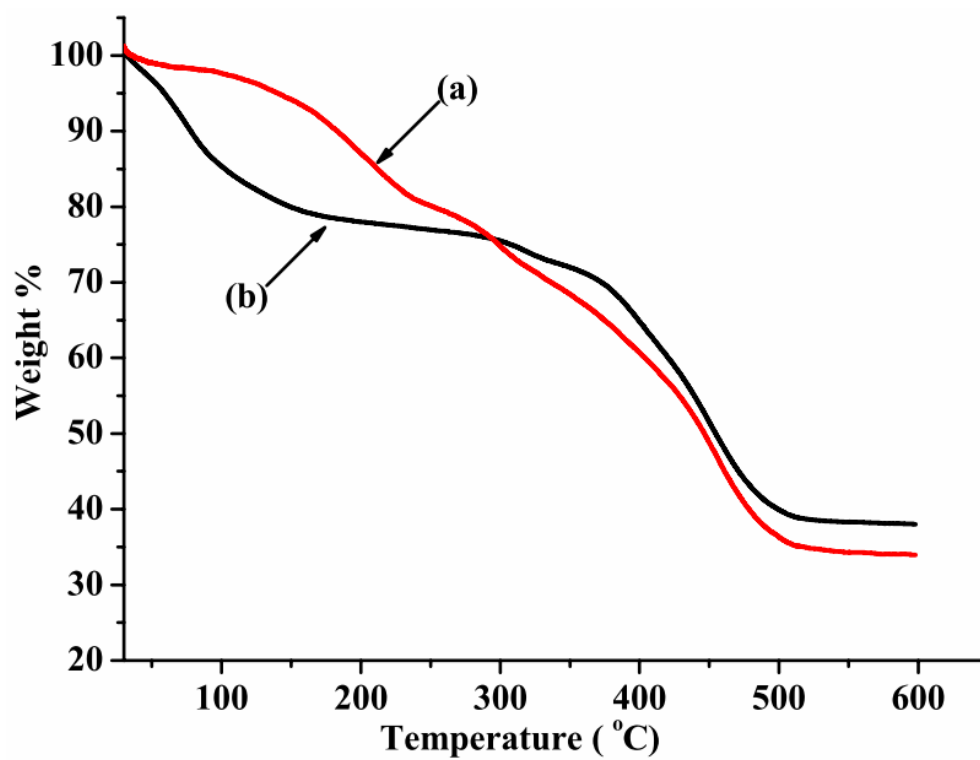
Figure S8. The TGA diagrams of **2** (a, red); The TGA diagrams of **2** soaked in MeOH (b, black).
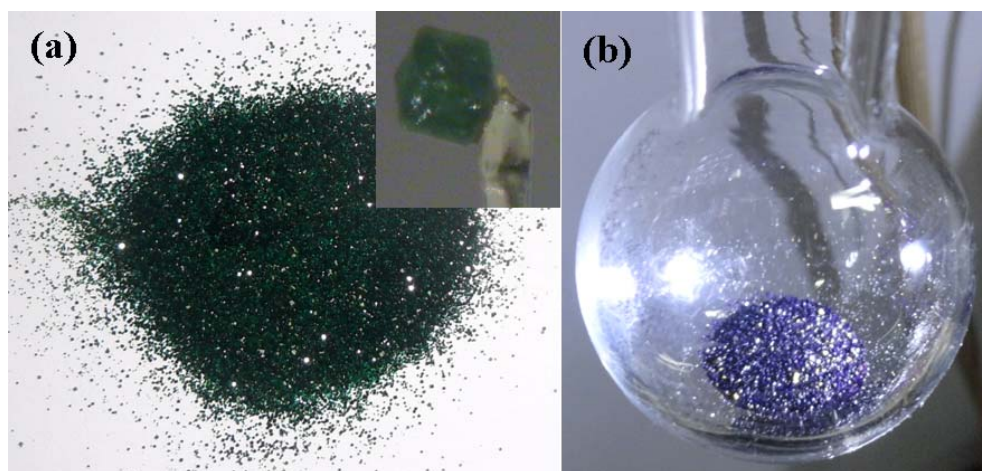

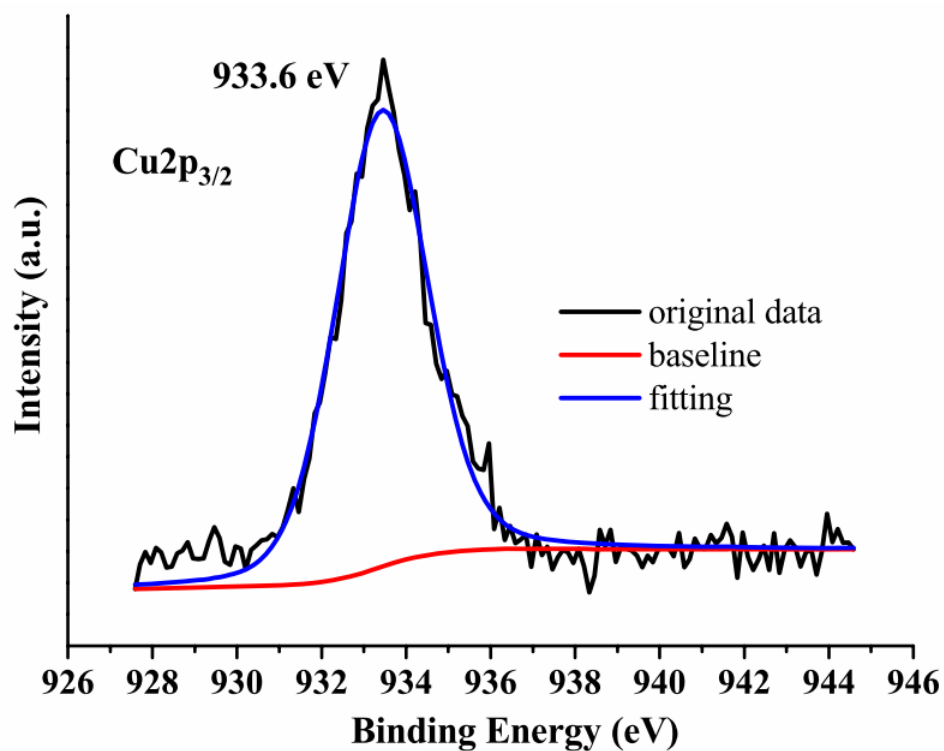Figure S9. The photographs of **2** (a); after degassing (b).

Figure S10. Cu2p$_{3/2}$ XPS spectra of **2**.

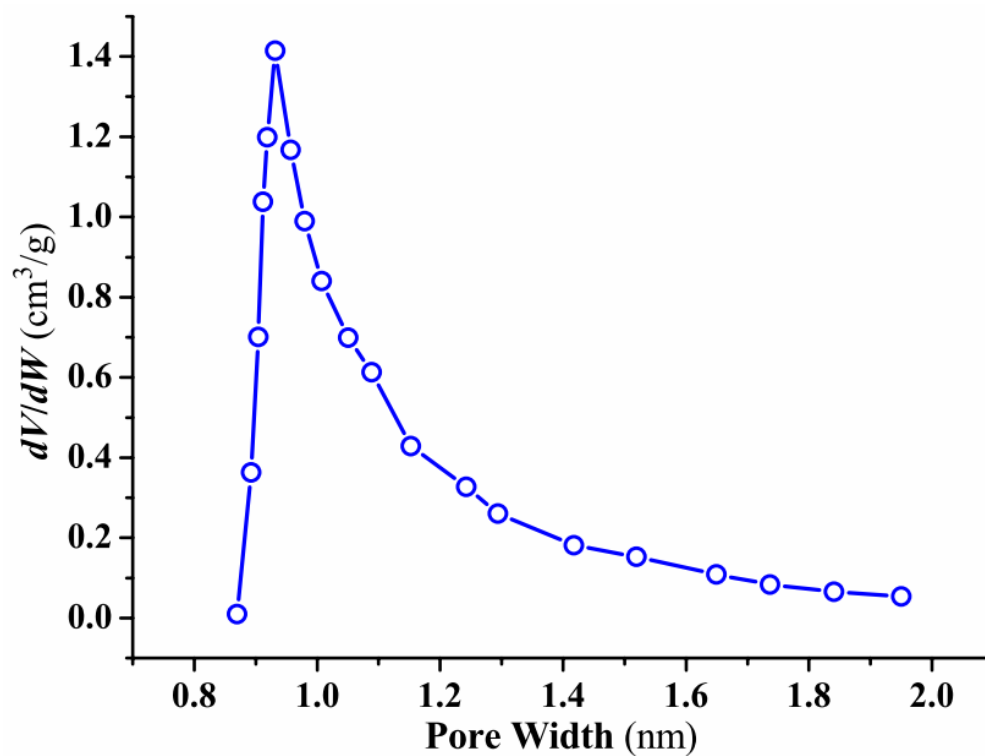Figure S10 shows the Cu2p$_{3/2}$ XPS spectra of **2** with the main component peak at 933.6eV, which should be attributed to Cu^{2+} ions.

Figure S11. Pore size distribution based on Horvath–Kawazoe (H–K) model.

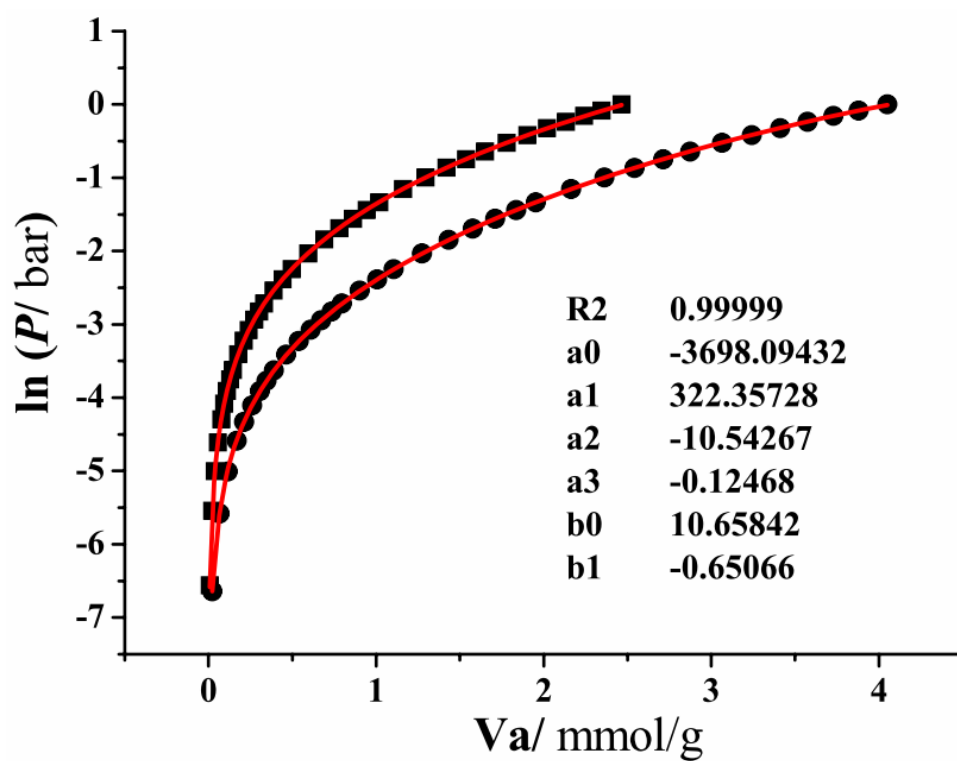| R2 | 0.99999 |
a0	-3698.09432
a1	322.35728
a2	-10.54267
a3	-0.12468
b0	10.65842
b1	-0.65066

Figure S12. CO_2 adsorption isotherms for **2** fitting by virial method.
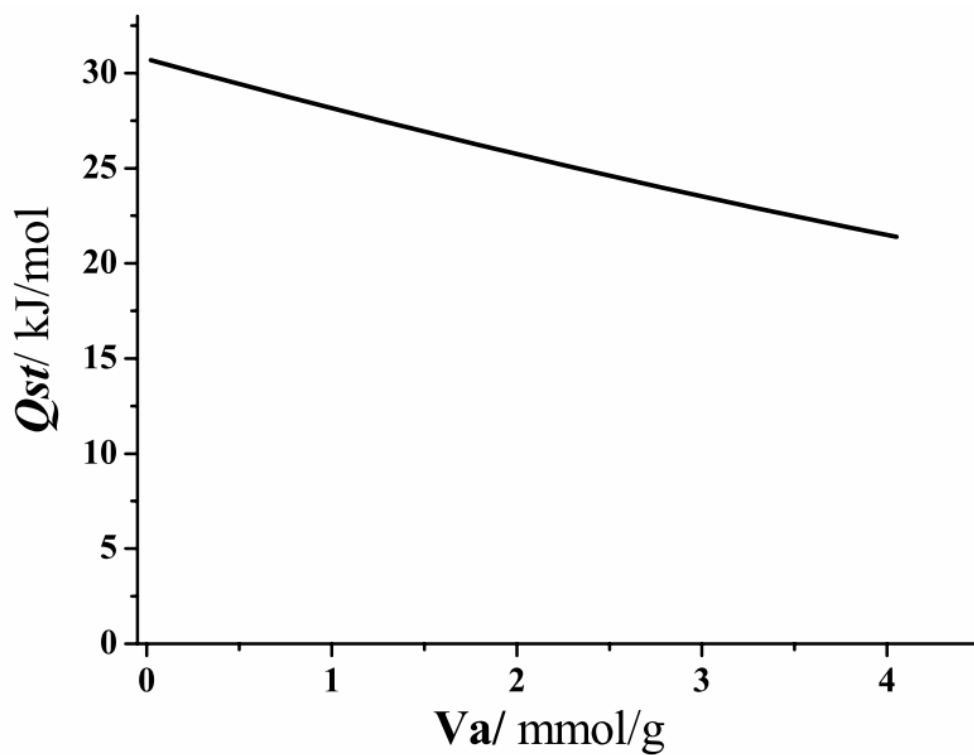
Figure S13. The isosteric heat of CO_2 adsorption for **2** estimated by the virial equation.

R2	0.99999
a0	-871.14952
a1	302.19357
a2	-167.40928
a3	206.11144
a4	-171.01893
a5	76.73996
a6	-13.61338
b0	8.33478
b1	-0.99222

Figure S14. H$_2$ adsorption isotherms for **2** fitting by virial method.

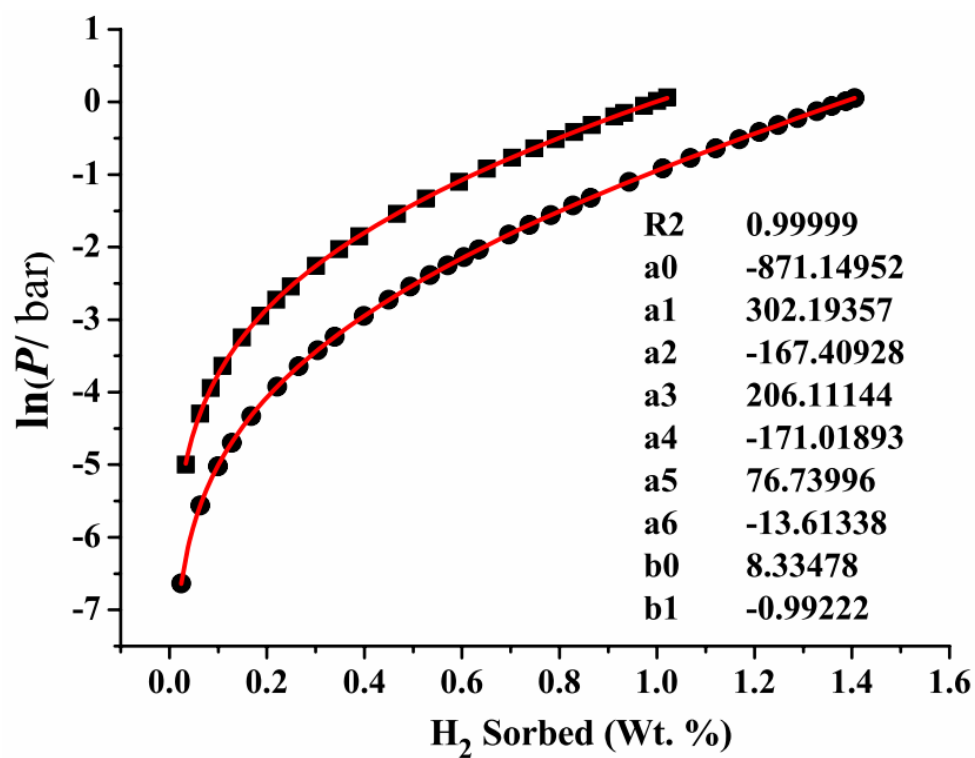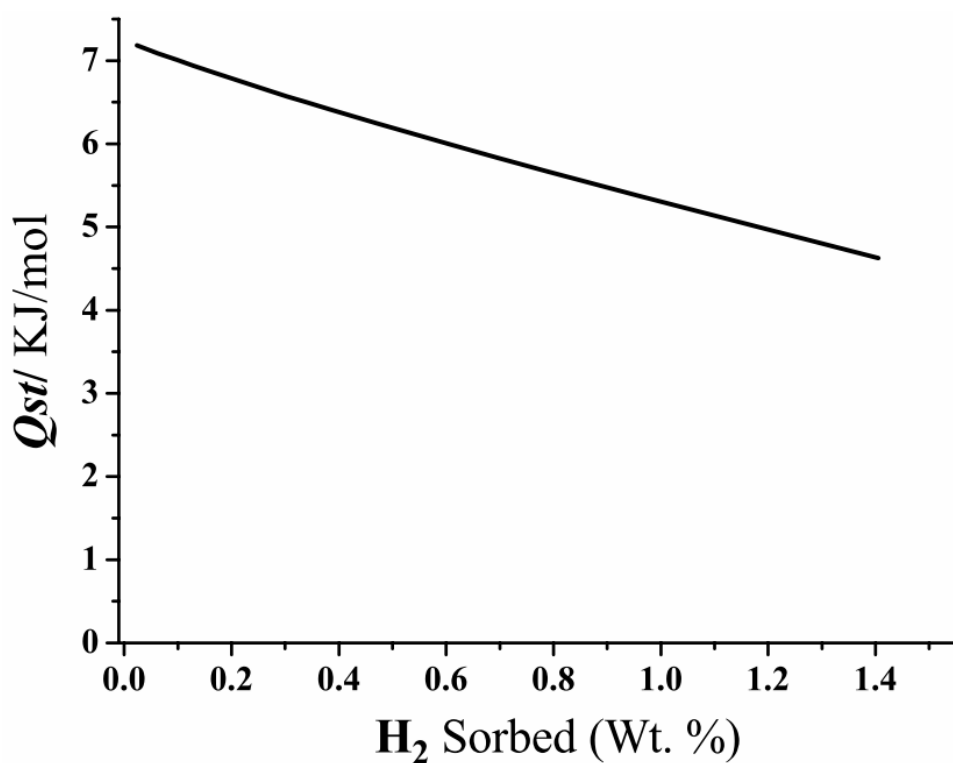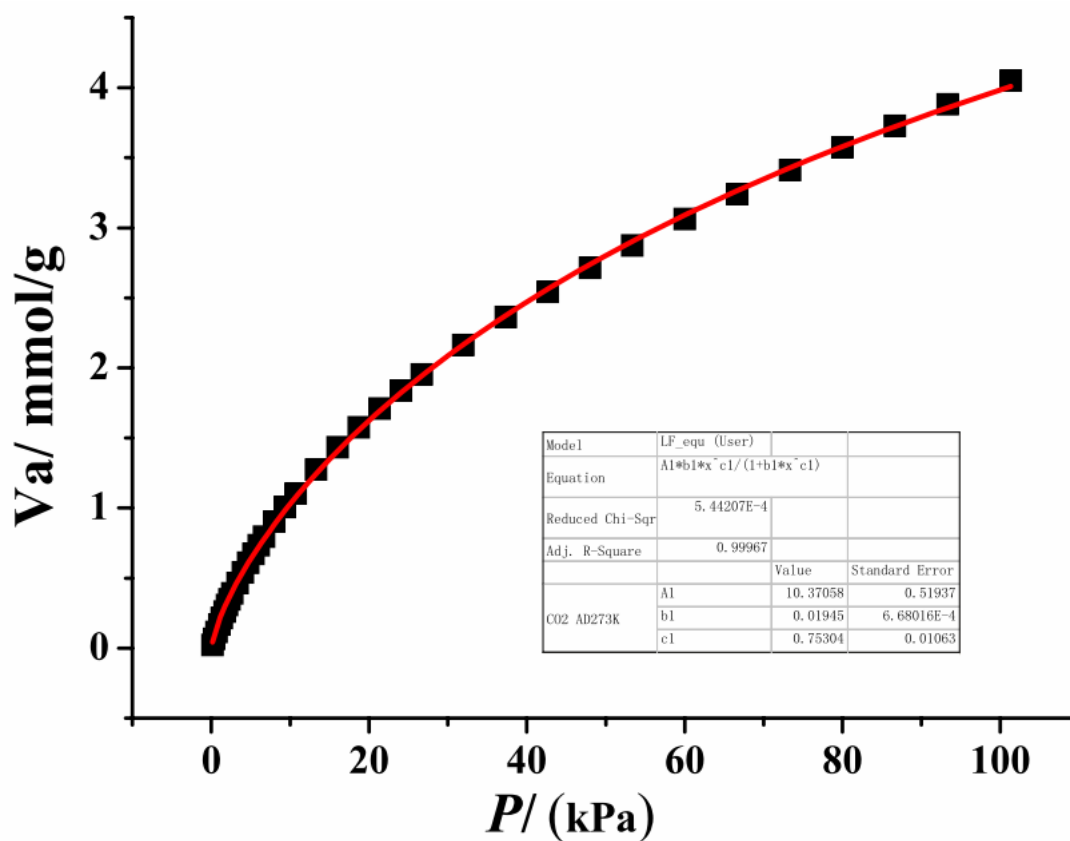Figure S15. The isosteric heat of H$_2$ adsorption for **2** estimated by the virial equation.

Model	LF_equ (User)		
Equation	A1*b1*x^c1/(1+b1*x^c1)		
Reduced Chi-Sqr	5.44207E-4		
Adj. R-Square	0.99967		
		Value	Standard Error
CO2 AD273K	A1	10.37058	0.51937
	b1	0.01945	6.68016E-4
	c1	0.75304	0.01063

Figure S16. CO_2 isotherm (black squares) and Langmuir-Freundlich fit (red line) for **2** at 273K.

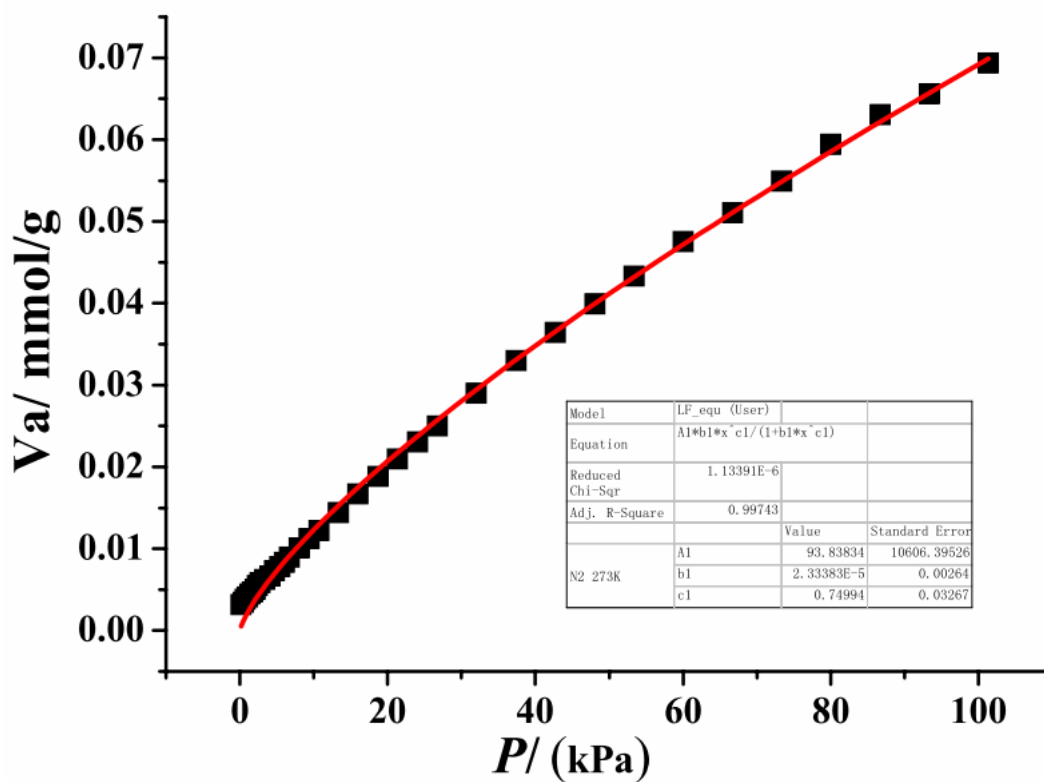| Model	LF_equ (User)		
Equation	A1*b1*x^c1/(1+b1*x^c1)		
Reduced Chi-Sqr	1.13391E-6		
Adj. R-Square	0.99743		
		Value	Standard Error
N2 273K	A1	93.83834	10606.39526
	b1	2.33383E-5	0.00264
	c1	0.74994	0.03267

Figure S17. N_2 isotherm (black squares) and Langmuir-Freundlich fit (red line) for **2** at 273K.
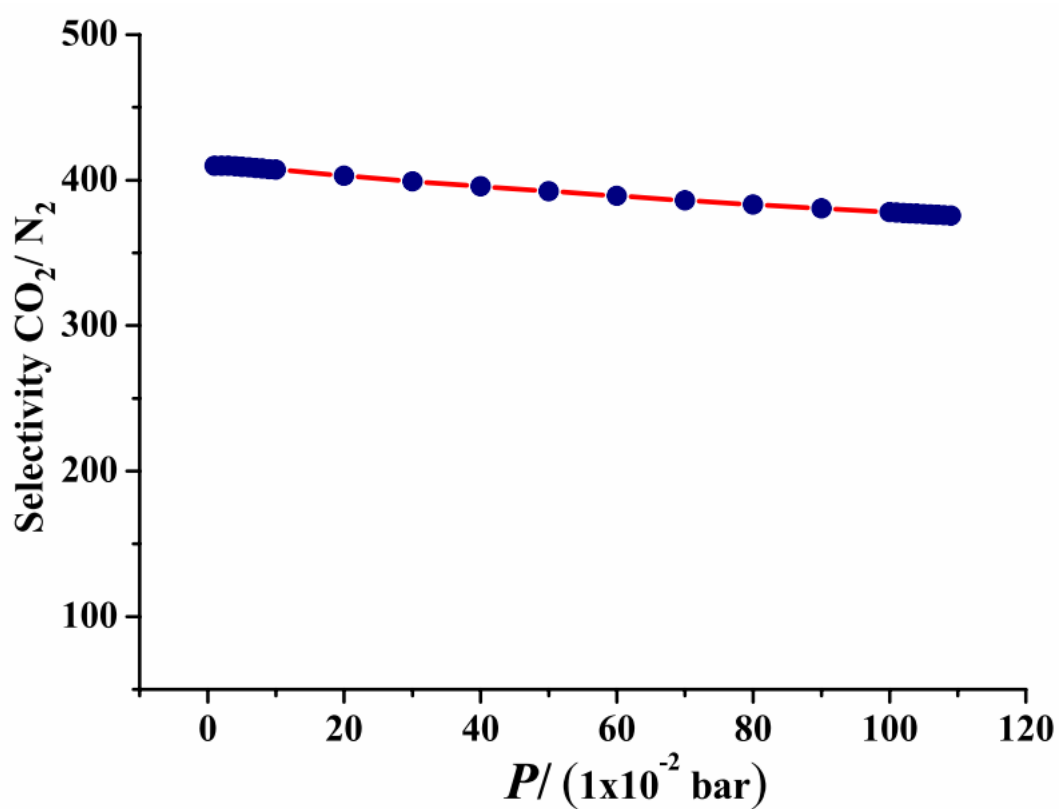
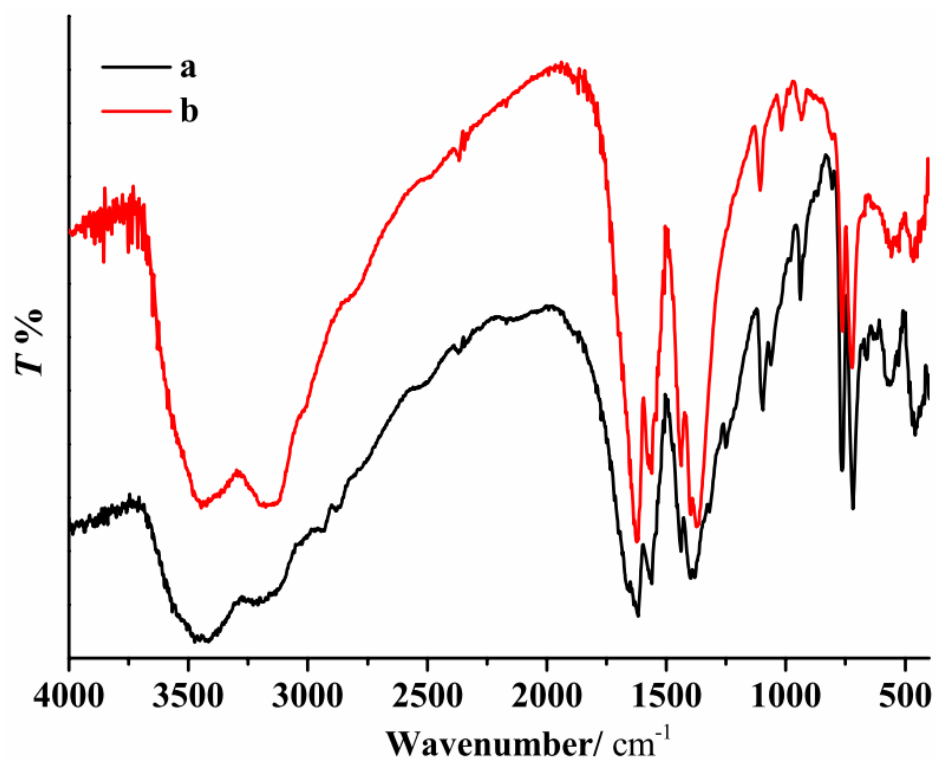Figure S18. IAST-predicted adsorption selectivity of the mixture of CO_2 and N_2 for **2** at 273K.

Figure S19. The IR spectras of compounds **1**(a) and **2**(b).
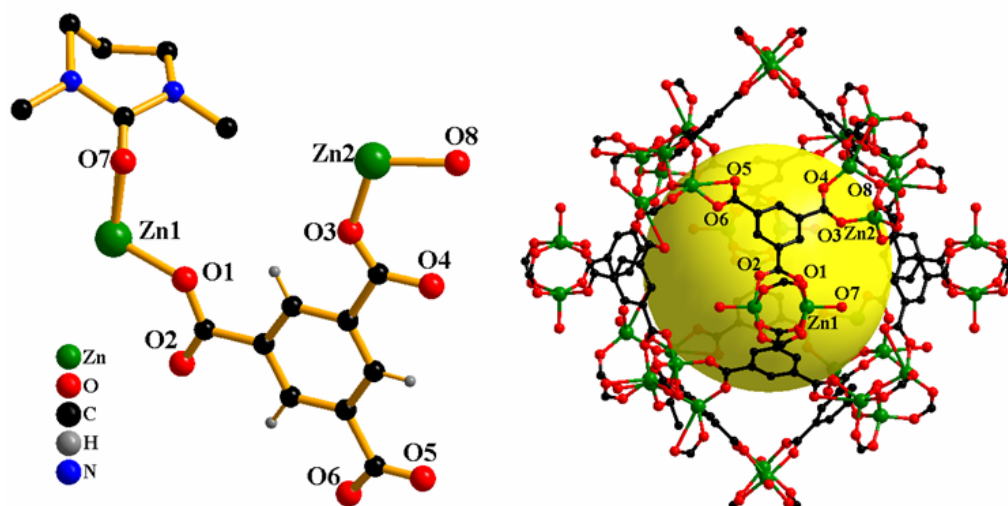
11

Figure S20. The asymmetric unit of **1** (a)**;** cavity generate by symmetry operations (b).